

Flexible Controls of Terahertz Waves Using Coding and Programmable Metasurfaces

Shuo Liu and Tie Jun Cui, *Fellow, IEEE*

(Invited Paper)

Abstract—In the first part of the paper, we make a brief review on the coding and programmable metasurfaces recently proposed at microwave and terahertz frequencies, which are realized by distributing coding particles “0” and “1” with opposite reflection phases on surfaces with certain coding sequences. The powerful manipulations to microwaves and terahertz waves using the coding and programmable metasurfaces are presented. In the second part of the paper, we propose a new coding scheme for the generation of ring-shaped radiation pattern. Different coding strategies are provided to demonstrate the flexible controls of the size, position, and number of rings in the radiation patterns, including changing the periodicity of the gradient coding sequence and adding it with one or multiple periodic sequences. A new structure featuring low electromagnetic interference and ultrahigh efficiency is designed to implement the ring-shaped pattern, which shows highly consistent results to the theoretical results calculated by Fourier transform. We remark that such a ring-shaped radiation pattern may find a wide range of applications in radar detections.

Index Terms—Metasurface, terahertz, manipulation, binary, coding, programmable, ring-shaped radiation.

I. INTRODUCTION

TAKING full controls of the reflections and transmissions of electromagnetic (EM) waves has been a research focus for a long time in both the physics and engineering communities, especially at light spectra, where lenses have been employed to focus light very well before the foundation of Maxwell’s equations. The wavefront controls using conventional devices, such as the dielectric lenses [1], [2] and reflector antennas [3]–[5], rely on the phase accumulation on the light path through either

the topology or the refractive index of natural material, which is typically limited to certain fixed values. Metamaterials, the artificially composite materials composed of subwavelength structures, have recently been demonstrated with the ability to tailor the permittivity and permeability arbitrarily, and further achieve unusual material properties and exotic EM responses which cannot be obtained from naturally occurring materials. It has experienced a rapid development in the past fifteen years, leading to many abnormal phenomena and a wide range of applications at frequencies ranging from the microwave to the optical spectra (e.g. negative refraction [6]–[8], subwavelength focusing [9]–[11], invisibility cloaking [12]–[15], refractive-index near-zero or epsilon-near-zero behaviors [16]–[18]). Although both permittivity and permeability of metamaterials could be artificially engineered, the metamaterial-based lens antennas are still designed and operated in the similar manner to the conventional dielectric lens antennas through the spatially varying profile of effective refractive index. As a consequence, the thickness of bulk metamaterials has to be larger than, or comparable to the operating wavelength, resulting in serious challenge for the fabrications of such bulk metamaterials at the terahertz and optical spectra using the current state-of-the-art three-dimensional (3D) micro/nano fabrication techniques [19], [20]. This has greatly hindered the development of 3D metamaterials at high frequencies.

Considering the aforementioned shortcomings of 3D metamaterials, it is highly desirable if the thickness of 3D metamaterials could be reduced to that of a surface. This has led to the emergence of metasurface [21], the two-dimensional (2D) form of metamaterial, which is composed of periodically or non-periodically arranged subwavelength scatterers on a thin (with deep subwavelength) surface. The ultrathin thickness of metasurfaces grants them great potentials for controlling EM waves with reduced metal and dielectric absorptions, light weight and easy fabrication, leading to the development of many practical devices at the terahertz and visible ranges such as the polarization convertor [22]–[24], perfect absorber [25]–[27], holography [28]–[30], modulator [31]–[33], and cloak [34], [35]. Recently, it has been demonstrated that metasurfaces could be used to realize anomalous reflections and refractions by imparting a controlled gradient of phase discontinuity over a single surface using the designed V-shaped plasmonic antennas [36]–[38].

Manuscript received June 14, 2016; revised August 4, 2016; accepted August 9, 2016. Date of publication August 10, 2016; date of current version December 1, 2016. This work was supported by National Natural Science Foundation of China under Grants 61302018, 61401089, 61401091, 61571117, 61501112, 61501117, and 61631007, the National Instrumentation Program under Grant 2013YQ200647, 111 Project (111-2-05), and the Natural Science Foundation of the Jiangsu Province (BK2012019).

S. Liu is with the State Key Laboratory of Millimeter Waves, Southeast University, Nanjing 210096, China, and also with the Synergetic Innovation Center of Wireless Communication Technology, Nanjing 210096, China (e-mail: liushuo.china@seu.edu.cn).

T. J. Cui is with the State Key Laboratory of Millimeter Waves, Southeast University, Nanjing 210096, China, and also with the Cooperative Innovation Centre of Terahertz Science, Chengdu 610054, China (e-mail: tjcui@seu.edu.cn).

Color versions of one or more of the figures in this paper are available online at <http://ieeexplore.ieee.org>.

Digital Object Identifier 10.1109/JSTQE.2016.2599273

Since the size of unit cell of metamaterial is typically in subwavelength scale, the metamaterial can be characterized as a homogeneous material with effective constitutive parameters, the electric permittivity and the magnetic permeability, using the effective medium theory [38], [39]. However, this theory no longer holds valid for the characterization of metasurface since the subwavelength thickness in the propagation direction does not meet the assumption of the periodical boundary condition. The modeling of metasurface experiences a tortuous road, from using the traditional effective medium theory [40], [41], then the surface susceptibilities [42], and finally the generalized sheet-transition conditions (GSTCs) [21].

All the aforementioned methods attempt to model the 3D/2D metamaterials with continuous constitutive parameters, which are analogous to the analogue circuits in which the signal varies continuously in a given range. In digital circuits, however, the information (signal) is discretized into only two different levels represented by distinct states ‘on’ and ‘off’. The quantization of the signal, though it is a simple step, has provided the digital circuits with many advantages over the analogue circuits, such as robustness to noise and easy design, and has led to the rapid developments of digital circuits since the last century. Inspired by the idea of signal discretization, we initially proposed the concept of coding metasurface [43] in 2014 by designing two different subwavelength coding particles (unit cells) ‘0’ and ‘1’ with opposite reflection phases 0° and 180° , respectively. The most convenient method to describe the material property of a coding metasurface is to use its reflection/transmission phases, which are unique and do not result in ambiguity that are associated with the conventional methods. By arranging coding particles on a 2D plane with the pre-designed coding sequences [43], various manipulations of coding metasurfaces to the microwaves have been demonstrated, such as the anomalous beam reflections and random diffusions. Later, the coding metasurfaces have been implemented in the terahertz frequency to realize broadband terahertz diffusions using the Minkovski fractal structures [44] and anomalous reflections with the ring resonators [45]. More recently, a polarization-controlled coding metasurface has been presented at the terahertz frequency using anisotropic coding particles, which could exhibit dual functions to the terahertz waves under orthogonal polarizations [46]. More interestingly, we have also proposed a principle called the scattering pattern shift which could rotate a radiation pattern to desired directions with little distortion [47], and revealed the relation between the coding pattern and radiation pattern by applying the Shannon entropy [48].

In this paper, we firstly make a brief review of the coding and programmable metasurfaces on their concepts, implementations, powerful manipulations to EM waves, and their extensions to the terahertz frequencies for random diffusions and polarization controlled manipulations using anisotropic structures. Then we propose a new coding scheme for generating ring-shaped radiation patterns. Nine different examples are given to demonstrate the versatile control of the ring-shaped pattern. As a practical implementation with real structure, we also design a new coding particle that has low EM interference and almost unity reflection.

II. A BRIEF REVIEW ON CODING AND PROGRAMMABLE METASURFACES

A. Coding Metasurfaces and Reflectarrays

Conventional reflectarray and transmitarray antennas [49], [50] have been well studied in the past decades and widely applied in the microwave frequencies for radar detections and satellite communications. From the viewpoint of functionalities, coding metasurfaces [43]–[46] are similar to reflectarrays, such as to generate single beam and multiple beams with controllable beam shape. Hence one may intuitively classify the coding metasurface as a type of reflectarrays. It is necessary to point out here the difference between the coding metasurface and reflectarray.

First, the size of unit cell for the coding metasurface is, in principle, from $\lambda/8$ to $\lambda/4$; while the size of unit cell for the reflectarray or transmitarrays is typically over half wavelength (not less than $\lambda/3$). Since the size of unit cells is much smaller than the operating wavelength, metamaterials can be equivalent to homogeneous or inhomogeneous materials. Likewise, coding metasurfaces composed of smaller coding particles are able to provide more accurate and uniform phase responses across the area of super unit cell [43] than the reflectarrays. This is due to the fact that the unit cells at the edge of super unit cell interact partially with adjacent unit cells having different geometries. Since such interactions are not taken into account in the simulation of a single unit cell with the periodic boundary condition, the reflection responses of unit cells in an encoded array may deviate from the desired value. Only the inner unit cells surrounded by identical ones could provide the ideal reflections. Therefore, such an undesired effect could be suppressed by incorporating more and smaller identical unit cells into one super unit cell.

Another benefit of smaller unit cell of coding metasurface is the capability of conversion from spatially propagating wave (PW) to surface wave (SW), which can be realized with a 2-bit coding metasurface when the periodicity of gradient coding sequence “00 01 10 11 . . .” is smaller than the free-space wavelength. However, it is impossible to implement the PW-SW conversion using the conventional reflectarray because the length of the gradient phase across 2π will be larger than one free-space wavelength, which is not able to provide sufficient wave momentum compensation required for the normal incident PW to be converted to SW.

Second, by adding a pin-diode in each coding particle, the coding states can be switched between “0” and “1” by simply turning the biasing dc voltage as “ON” and “OFF”, respectively, serving as a programmable metasurface [43]. This is in sharp contrast to the phased array antennas that employ the phase shift technology, in which complex circuits are always required to compensate for the distribution losses in the feeding network, leading to high cost and larger weight than the programmable metasurface design. Moreover, the use of transmission line in the phase shift circuit becomes increasingly lossy at higher frequencies (e.g. millimeter-wave frequency). The pin-diode switches used in the programmable metasurface, however, could operate at relatively higher frequencies (more than 60 GHz) with reduced loss and much simplified feeding network. As the fre-

quency further increases to the terahertz frequency, where the pin-diodes may not be commercially available, some materials such as doped silicon [32], [51] and vanadium dioxide (VO₂) [52], [53] could be considered as the active part of the programmable metasurface.

Third, it is worthwhile to point out that the main purpose of introducing the coding metasurface is not solely limited to the generation of single or multiple beams with controllable shapes and directions. Our aim on the quantization of the continuous phase profile is to establish a bridge linking the physical electric field with the discrete digital codes, which can be processed with many existing algorithms from the information theory (e.g. digital image processing) to enable more versatile manipulations of EM waves and unusual physical phenomena. It is well known that the near field is connected with its far-field scattering pattern through the linear operation of the Fourier transform. Hence, there must be potential relations between the coding pattern and the radiation pattern which may be of particular interests in certain applications. For example, we proposed to measure the information of coding metasurface using Shannon entropy, and set up an analytical connection between the coding pattern of an arbitrary coding metasurface and its far-field pattern [48].

We should also note that the concept of digital metamaterial proposed in Ref. [54] is different from that of coding and programmable metamaterials, in which a methodology has been introduced to produce new materials with controllable permittivity by mixing two different materials (metamaterial bit) with certain proportions (metamaterial byte). For the coding metasurface, the word “coding” is used to denote the coding sequence, determining the arrangement of coding particles with a limited number of known states (coding digits) in the 2D array. Different coding sequences carry different information, which are reflected by their radiation patterns.

B. Principle Design of the Coding and Programmable Metasurfaces

Different from the conventional metamaterials that effective medium parameters are designed continuously within a certain range of values, the coding metasurfaces manipulate the EM waves through a sequence of a limited number of known states, as is schematically illustrated in Fig. 1(a) and (b) by a 1-bit case with two different coding sequences [43]. The normally incident wave will be reflected to two symmetrically oriented directions in the upper half space by the periodic coding sequence “01010101...” (see Fig. 1(a)), while is split in four directions (see Fig. 1(b)) as the coding sequence becomes a chessboard distribution. In order to implement the discrete coding digits “0” and “1” at the microwave frequency, the structure shown in the upper-right inset of Fig. 1(c) is designed as the unit cell, which is composed of a metallic square patch and a ground sheet separated by a dielectric spacer ($\epsilon = 2.65$, $\delta = 0.001$). It can be observed from the reflection phases in Fig. 1(c) that the phase difference ranges from 135° to 200° from 8.1 to 12.7 GHz, and is exactly 180° at 8.7 and 11.5 GHz [43].

The powerful manipulations of EM waves through various coding sequences will be shown in the following sections. Here,

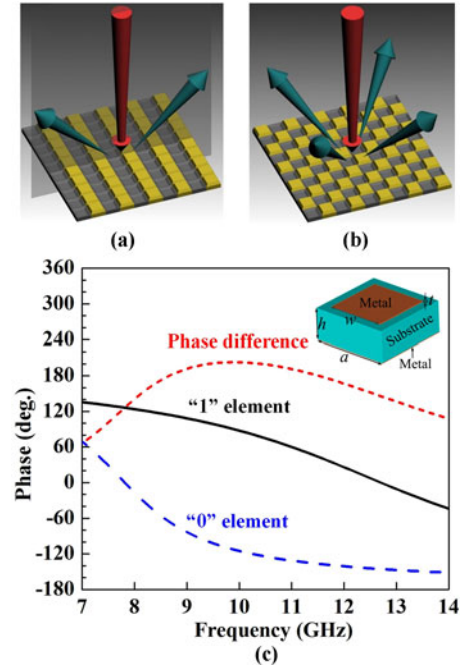


Fig. 1. (a) and (b) The schematic illustration of the powerful manipulation of EM wave for the coding metasurfaces encoded with two different coding sequences, “010101...” and the chessboard distribution. (c) Phases of reflection spectra of the “0” element, “1” element and their phase difference. The upper-right inset shows the structure of the coding element.

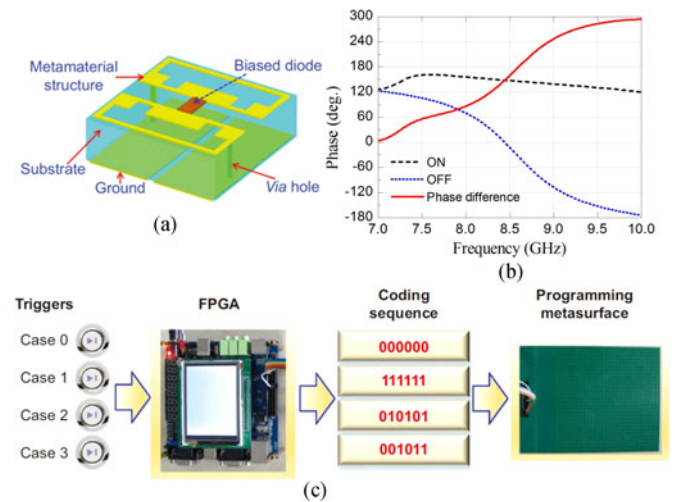


Fig. 2. (a) The structure of the coding particle for the programmable metasurface [43]. The digital state can be electrically switched between ‘0’ and ‘1’ when the PIN diode is biased ‘OFF’ and ‘ON’, respectively. (b) Reflection phase spectra when the PIN diode is turned ‘OFF’ and ‘ON’ and the phase difference between them. (c) A flow diagram for the programmable metasurface controlled by a FPGA hardware.

we first present the realization of programmable metasurface [43], in which the coding digits “0” and “1” can be electrically controlled by adding a PIN diode between two metallic patches, as is shown by the structure in Fig. 2(a). When the effective capacitance of PIN diode is turned “on” and “off”, the coding element will react differently to the illuminating wave, as can be observed from the curves of reflection phases (see Fig. 2(b))

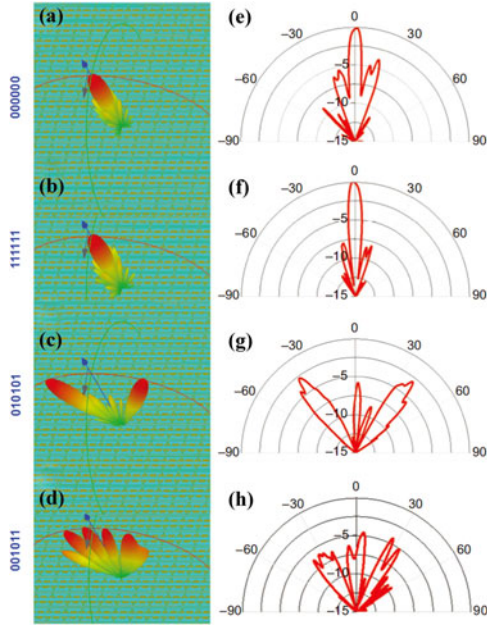


Fig. 3. (a)–(d) The numerically simulated scattering patterns at 8.3 GHz for the programmable metasurfaces with different coding sequences: (a) “000000”, (b) “111111”, (c) “010101”, and (d) “001011”. (e)–(h) The experimentally measured scattering patterns at 8.6 GHz for the programmable metasurfaces with different coding sequences: (e) “000000”, (f) “111111”, (g) “010101”, and (h) “001011” [43].

at the “on” and “off” states [43]. Their phase difference reaches approximately 180° from 8.3 to 8.9 GHz, thus functioning as an active coding particle for the 1-bit programmable metasurface.

A field programmable gate array (FPGA) was employed in the experiment to digitally input the coding sequences to the programmable metasurface (see Fig. 2(c)). Fig. 3 provides the measured scattering patterns when the coding sequences input from FPGA are set as “000000” and “111111”. For the coding sequences “000000” and “111111”, there is only one scattering beam at the backscattering direction due to the uniform phase distribution across the entire 2D plane. For the “010101” coding sequence, the normal incidence is split into two beams with equal angle with respect to the normal axis, whereas it becomes multiple beams for “001011” coding sequence [43]. Recently, the programmable metasurface has been further extended to be fed by a point-source excitation, resulting in new-concept radars [55].

C. Broadband Diffusions of Terahertz Waves With Random Coding Sequences

In addition to the aforementioned functionalities realized by the periodic coding sequences, we demonstrated that, with random coding sequences [43], [44], the normal incidence can be diffused in numerous directions in the upper-half space (see Fig. 4(a)), and thus we can effectively reduce the radar cross section (RCS) at the backscattering direction [44]. In order to reduce the size of coding particle as well as increase the working bandwidth, a Minkowski loop featuring the fractal geometry and excellent self-similar property is utilized for the coding particle design (see the inset of Fig. 4(a)) [44]. Fig. 4(b) shows the de-

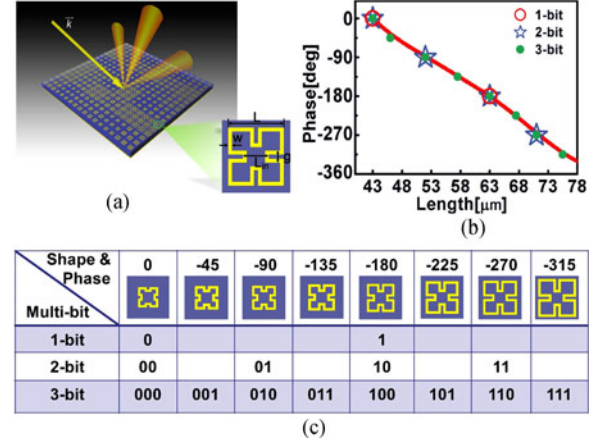


Fig. 4. (a) Conceptual illustration of the broadband diffusion of THz wave using the random distribution of the Minkowski coding particles. (b) The phase variation as a function of the loop width L . (c) The structures of the designed 1-, 2-, and 3-bit coding particles [44].

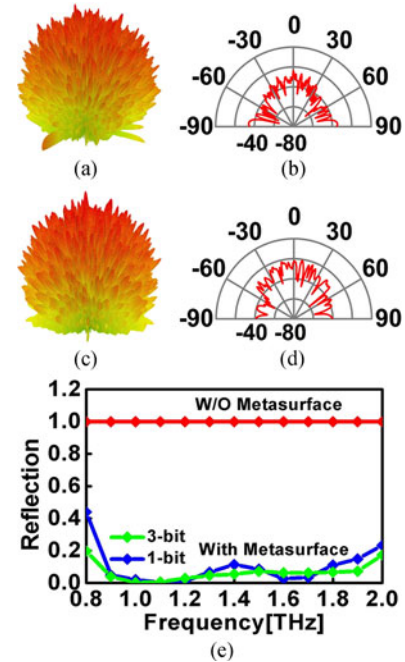


Fig. 5. (a) and (b) The 3D and 2D scattering patterns of the 1-bit coding metasurfaces at 1.1 THz. (c) and (d) The 3D and 2D scattering patterns of the 3-bit coding metasurfaces at 1 THz. (e) The simulated reflections in the backscattering direction of the 1-bit, 3-bit coding metasurfaces and the PEC case in the frequency range from 0.8 to 1.2 THz [46].

pendence of simulated reflection phase on the loop width L . It is clear that the phase decreases almost linearly from 0° to -315° as L increases from 43 to $75.5 \mu\text{m}$. By quantizing the continuous 2π phase range into 2, 4, and 8 equally-spaced discrete phases, we obtain the 1-bit, 2-bit, and 3-bit coding particles as displayed in Fig. 4(c).

The diffusion effects of terahertz waves are demonstrated in Fig. 5 with the 1-bit and 3-bit coding metasurfaces. Both models include 7056 Minkowski coding particles and cover the same area of $7.56 \times 7.56 \text{ mm}^2$ ($25.2 \times 25.2 \lambda^2$ at 1.0 THz).

Fig. 5(a) and (c) show the 3D scattering patterns of the 1-bit and 3-bit coding metasurfaces under the normal illumination at 1.0 and 1.1 THz, respectively. It is clear that the random coding sequence in both cases could effectively redistribute the EM energy to multiple directions, as are further verified from the 2D E-plane scattering in Fig. 5(b) and (d). In the experiment, the fabricated samples show not only highly consistent results to the simulations under the normal illuminance, but also an excellent diffusion effect under the oblique incidence from 20° to 40° over a relatively broad bandwidth. The performance of the broadband RCS reduction at the backscattering direction for the 1-bit and 3-bit cases are presented in Fig. 5(e), where the reflections reflected by the coding metasurface (blue and green lines) are less than 10% of that from the PEC board with same dimension (red line), indicating an ideal material for broadband RCS reduction at terahertz frequencies. Although the RCS reduction behaviors in Fig. 5(e) for the 1-bit and 3bit cases are similar, we remark that the 3-bit coding metasurface with fully optimized coding sequence will be much superior to the 1-bit coding metasurface in diffusing the EM waves.

D. Anisotropic Coding Metasurface

It is well known that metamaterials, like any natural EM materials, can be classified as isotropic and anisotropic cases depending on their effective medium parameters. In the isotropic metamaterials, the medium parameter is a scalar, which is insensitive to the polarization; whereas in the anisotropic metamaterials, the medium parameter becomes a tensor, which is sensitive to the polarization. Based on the same logic, the coding metasurfaces should also be classified into two types: isotropic coding metasurfaces and anisotropic coding metasurfaces. In fact, the coding metasurfaces discussed in Sections II-B and II-C belong to the isotropic coding metasurfaces. Recently, we proposed the concept of anisotropic coding metasurface at terahertz frequencies that could exhibit distinct functionalities for different polarizations [46]. Fig. 6(a) and (b) schematically illustrate the polarization-controlled behaviors of the anisotropic coding metasurfaces, in which the normal incidence will be anomalously reflected to the left-hand side under the x polarization, while to the right-hand side under the y polarization.

To realize the independent digital states under orthogonal polarizations, the dumb-bell shaped structure displayed in Fig. 6(c) is designed as the anisotropic coding particle [46] (the gold ground sheet is not shown in Fig. 6(c)), with the corresponding reflection phases plotted in Fig. 6(d). It is clear that the phase difference between the x - and y -polarizations equals 180° at the operating frequency of 1.0 THz due to its anisotropic geometry. Fig. 6(e) shows the sixteen coding particles that are required to build the 2-bit anisotropic coding metasurfaces. The four structures on the diagonal line are simply the square patches due to the identical phase responses under the x - and y -polarizations. The six anisotropic elements in the upper triangular area are the 90° rotation of those in the lower triangular area.

Fig. 7(a) and (b) show the 3D scattering patterns for the 2-bit anisotropic coding matrix M_a , which is formed by combining

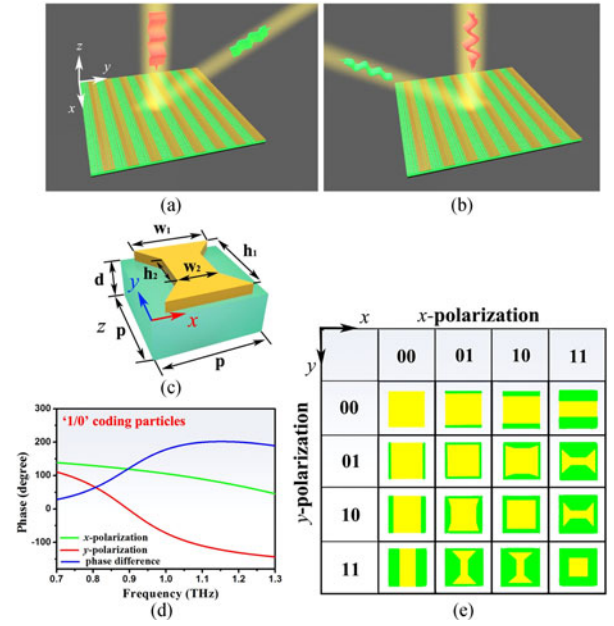


Fig. 6 (a) and (b) The illustrations for the dual-functionality of the anisotropic coding metasurface, which can anomalously reflect the normal incident beam to the right side under the x -polarization, and to the left side under the y -polarization. (c) The structure of the anisotropic coding particles '1/0' (without the metallic background). (d) Reflection phases and the corresponding phase difference for the anisotropic coding particles '1/0' under the x - and y -polarizations. (e) The structures of the sixteen coding particles for the 2-bit anisotropic coding metasurface [46].

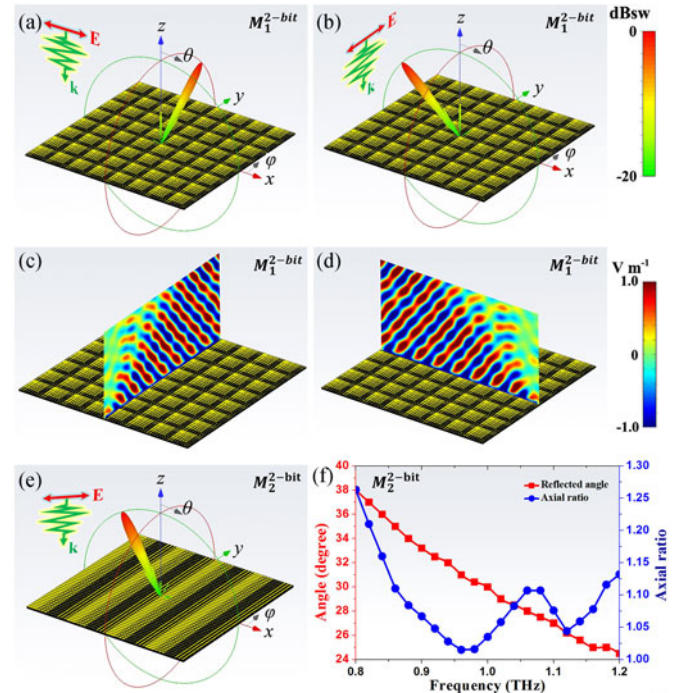


Fig. 7. (a) and (b) The 3D far-field scattering patterns for the metasurfaces encoded with coding matrix M_a under the x - and y -polarizations. (c) and (d) The corresponding near-electric-field distributions E_x and E_y components on the $y-z$ and $x-z$ cutting planes. (e) The 3D far-field scattering patterns for the metasurface encoded with coding matrix M_b when the incident terahertz wave is linearly polarized by 45° with respect to the x -axis. (f) The maximum radiation direction (red square line) and the axial ratio (blue circle line) of the circularly polarized wave as the frequency ranges from 0.8 to 1.2 THz.

two coding sequences “01230123...” that vary along the x and y directions. We remark that ‘0’, ‘1’, ‘2’, and ‘3’ represent the binary codes ‘00’, ‘01’, ‘10’, and ‘11’, respectively. As expected, the x -polarized normal incidence is anomalously reflected to the direction of ($\varphi = 90^\circ$, $\theta = 48^\circ$) in the y - z plane (see Fig. 7(a)); while for the y -polarization, however, it is redirected to the direction of ($\varphi = 180^\circ$, $\theta = 48^\circ$) in the x - z plane (see Fig. 7(b)). The anomalously reflected wave under the x and y directions can be clearly visualized from the electric field distributions in Fig. 7(c) and (d), respectively. The almost identical electric field distributions in both figures indicates an excellent isolation of the coding digits between the x - and y -polarizations, which enables the THz wave to be independently controlled under orthogonal polarizations.

Interestingly, the 2-bit anisotropic coding metasurface can be utilized to design a background-free reflection-type quarter-wave plate that could convert the linearly polarized wave to circularly polarized wave and reflects it to an anomalous direction. The anisotropic coding matrix M_b is obtained by setting the coding sequences under the x - and y -polarizations as “01230123...” and “12301230...”, respectively. As each coding particle has 90° phase difference between the x - and y -polarizations and almost unity amplitudes, the scattered wave becomes purely circular polarization in the radiation direction. Fig. 7(f) plots the axial ratio (blue line) of the circularly polarized wave at the maximum radiation direction (red line) from 0.8 to 1.2 THz, which is only about 1.03 at 1.0 THz and smaller than 1.26 over the entire bandwidth. Such a perfect circular polarizer featuring high-efficiency and flat profile may be potentially applied in the terahertz systems to serve as a reflection-type quarter-wave plate.

III. RING-SHAPED RADIATION PATTERN USING CODING METASURFACES

A. Concept and Performance

We have demonstrated in the previous works various periodic coding patterns that could generate differently-shaped radiation patterns [43], [46], including the single-beam pattern (2bit, “01230123...”), two-beam pattern (1-bit, “01010101...”), and the four-beam pattern (1-bit, chessboard distribution). For those coding schemes, as the coding digits vary along either the x - or y -axis with finite length, the resulting scattering beams are restricted in the small range of angle in the azimuthal direction (φ -axis in the spherical coordinate). These types of radiation patterns are typically with high directivity, and are suitable for the applications of long-range or high-sensitivity radar detection. Another type of antenna is called as omnidirectional antenna, which radiates uniformly in the azimuthal direction [56]–[59]. Because most EM powers are radiated equally in all azimuthal directions (commonly close to horizontal directions), instead of being wasted upwards to the sky or downwards to the earth, the omnidirectional antennas are desired for certain applications such as radio broadcasting, cellular base station, and wireless local area network. So, an important question arises: whether, in principle, an omnidirectional radiation pattern can be realized with the coding metasurface? The answer is definitely

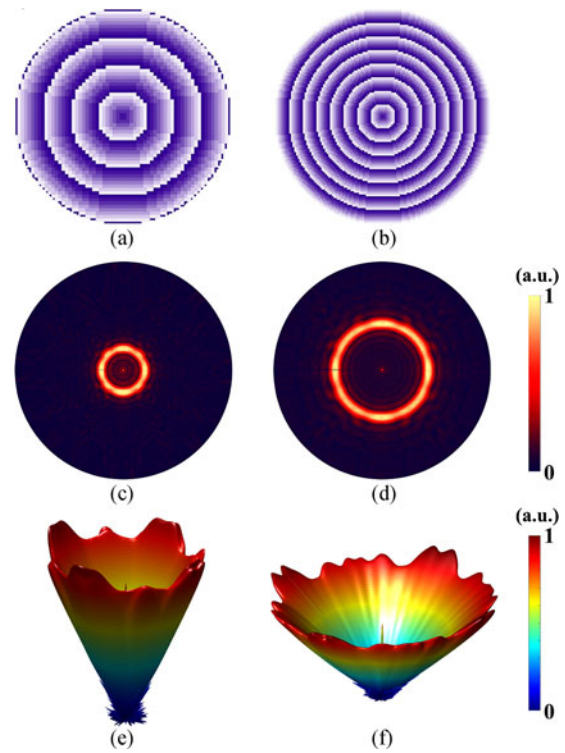


Fig. 8. (a) and (b) The coding patterns for M_1 and M_2 . (c) and (d) The 3D radiation patterns expressed in the polar coordinate system. (e) and (f) The 3D radiation patterns expressed in the spherical coordinate system.

yes. By varying the gradient coding digits along the radial direction, we are able to generate, for either linear or circular polarization, an omnidirectional radiation in a desired range of elevation angle. Different from the conventional high-gain omnidirectional antennas [56], [57] which commonly radiate in the horizontal plane ($\theta = 0^\circ$), the cone-shaped radiation patterns enabled by the coding metasurface can be designed to scan in the upper-half space from $\theta = 0^\circ$ to 90° . Most importantly, we will demonstrate in the following the powerful manipulations of the coding metasurface in controlling the shape, direction and number of cone-shaped radiation pattern, by adding one or multiple periodic coding sequences that vary along the x - and/or y -axes. Compared with the conventional omnidirectional antennas using the electrically-small microstrip patch antenna [54], leaky-wave antenna [58], and biconnical antenna [59], coding metasurfaces provide more powerful control on the shape of omnidirectional radiation patterns and flexible design with reduced complexity.

Fig. 8(a) shows the coding pattern M_1 designed to generate the ring-shaped radiation pattern. It is formed by arranging the 3-bit coding particles on a round area with the gradient coding sequence “0123456701234567...” along the radial direction, which will be denoted as S_1 in the following. The coding digits “0” to “7” represent the reflection phases of 0° , 45° , 90° , 135° , 180° , 225° , 270° and 315° , respectively, which is indicated in each coding pattern by the bright level of the purple color. As the coding digit is a linear gradient along the radial direction, we observe a series of concentric rings from the coding pattern.

Similar to the previous works, each coding digit here is composed of $N \times N$ identical coding particles ($N = 2$ for M_1). The diameter of the round coding metasurface equals the length of 128 coding particles. The reason why the coding particles are arranged in the round area instead of the square area is simply because the gradient direction here is along the radial axis. The number of coding digits must be the same in all azimuthal directions to have equal scattering intensity in the azimuthal direction.

To obtain the radiation pattern for a given coding pattern, we present here a fast approach for calculating the 3D scattering pattern directly from the coding pattern, which primarily involves a 2D FFT operation of the coding pattern and a coordinate transformation from the angular coordinate (u, v) to the visible angle coordinate (θ, φ) using the following equations,

$$u = \frac{2\pi}{\lambda} d_x \sin \theta \cos \varphi \quad (1)$$

$$v = \frac{2\pi}{\lambda} d_y \sin \theta \sin \varphi \quad (2)$$

where d_x, d_y denote the periodicities of the coding particle along the x and y directions, respectively; (u, v) range from 0 to π . According to Eqs. (1) and (2), d_x and d_y must be designed less than half wavelength in order to let the metasurface scan in the entire upper-half space. In the calculation, the working wavelength λ is set as $1250 \mu\text{m}$ (0.24 THz), and the amplitude is assumed as unity across the square area ($250 \times 250 \mu\text{m}$) of each coding particle. We remark that this approach can significantly reduce the computational complexity and produce the results in only a couple of seconds. This is in big contrast to the time (at least three orders of magnitude longer) took by the numerical simulations using the commercial software, CST Microwave Studio.

The 3D far-field scattering pattern calculated using the above approach is plotted in Fig. 8(c) with the polar coordinate system, in which the radial and azimuthal directions represent the elevation angle θ and azimuthal angle φ in the spherical coordinate, respectively. Note that the brightness in the 3D scattering pattern indicates the radiation intensity, which has been normalized to the maximum intensity of each plot. An obvious ring can be observed from the 3D scattering pattern in Fig. 8(c), implying that most of the EM energy is concentrated inside a certain range of angle in the elevation plane and radiates almost uniformly in the azimuthal direction. The radiation pattern can be visualized more straightforward by plotting it in the spherical coordinate system, as shown in Fig. 8(e), where a cone-shaped radiation pattern can be clearly observed. An ascending order coding sequence is used in this work, i.e. the phase of coding particles increases as they leave away from the center, to generate the ring-shaped radiation pattern in the far field. We note that the same coding sequence can also be used to generate the Bessel beam in the near field. However, if we reverse the coding gradient of coding sequence as “7654321076543210...”, we could obtain the ring-shaped radiation patterns in the far field. In this situation, the near field will no longer be the Bessel beam distribution. The fluctuation of radiation intensity observed in the azimuthal radiation (as φ varies from 0 to 2π) is caused by

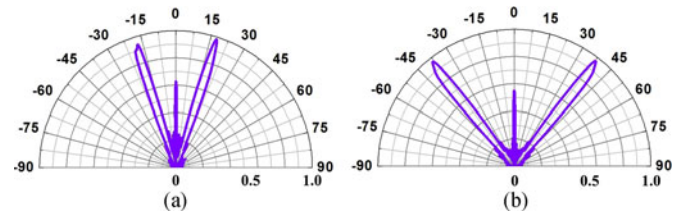


Fig. 9. (a) and (b) The radiation patterns plotted in the E-plane for M_1 and M_2 .

the following reasons. The coding particles are arranged along the x and y axes in the Cartesian coordinate, which inevitably leads to an approximation error of the round area. This can be verified from the flat phase edges at the four directions $\pm x$ and $\pm y$. Second, the serrated boarder of the concentric ring in the coding pattern, resulted from the finite size of the coding particle, can also contribute to such slight non-uniformity in the azimuthal direction. However, reducing the size of coding particles as well as aligning them in the polar coordinate system could help improving the uniformity of radiation intensity in the azimuthal direction.

In order to characterize the omnidirectional radiation in the elevation plane, we plot in Fig. 9(a) the 2D scattering pattern in the E-plane. It can be observed that the maximum radiation direction appears in the direction of 17.5° , which agrees with the theoretical value of 18.2° calculated by the generalized Snell's law [37]. The slight discrepancy could be attributed to the aforementioned approximation error of the concentric rings.

Based on the generalized Snell's law, one can increase the elevation angle of the omnidirectional radiation by simply decreasing the periodicity of the gradient coding sequence along the radial direction. We verify this idea by setting the super-unit-cell size $N = 1$ for the S_1 coding sequence, and the resulting coding pattern M_2 is shown in Fig. 8(b). Clearly, the variation rate of the periodic sequence becomes faster than that in Fig. 8(a). As expected, the diameter of the ring in the calculated radiation pattern (see Fig. 8(d)) is bigger than that in Fig. 8(c), which indicates that the EM energy radiates at larger elevation angle. We can clearly observe from Fig. 8(f) that the opening angle of the cone-shaped scattering pattern is larger than that in Fig. 8(e). The 2D scattering plotted in the E-plane shows that the elevation angle of maximum radiation appears at 38.1° , which is again in accordance with the theoretical result of 38.6° .

Here, we present another interesting coding pattern M_3 (see Fig. 10(a)) by compressing the coding pattern M_1 along the vertical direction. Now, the periodicity of the gradient coding sequence along the vertical direction becomes 8, while for the horizontal direction, it still remains 16. This transformation results in an ellipse-shaped coding pattern (see Fig. 10(a)). The resulting radiation pattern in Fig. 10(b) shows an elliptical-ring-shaped pattern, which means that the elevation angle of the radiation varies as an elliptical function of the azimuthal direction. According to the generalized Snell's law, the elevation angle of the maximum radiation along the horizontal and vertical directions should be equal to those of M_1 and M_2 . Such a conjecture is verified by the 2D plots of scattering patterns on the H-plane

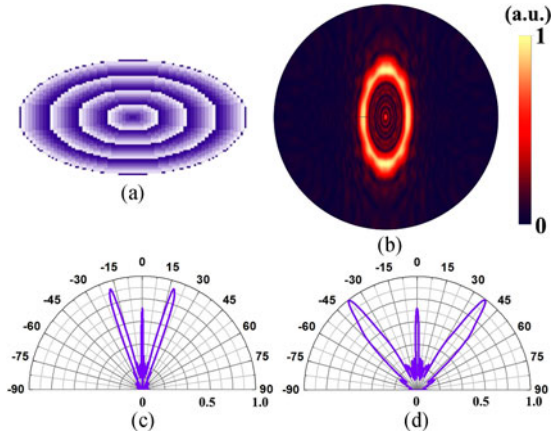


Fig. 10. (a) and (b) The coding pattern and radiation pattern for M_3 . (c) and (d) The radiation patterns in the H-plane and E-plane.

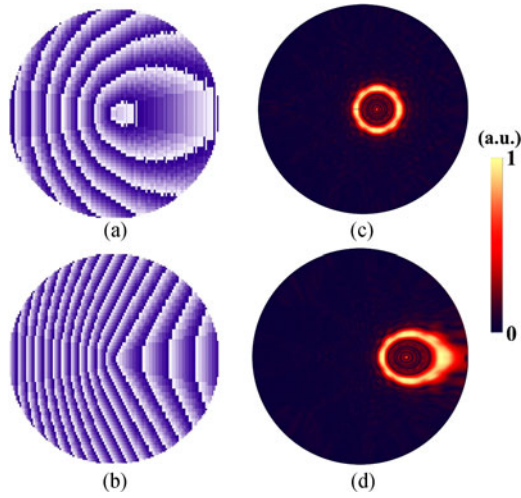


Fig. 11. (a) and (b) The coding patterns for M_4 and M_5 . (c) and (d) The 3D radiation patterns for M_4 and M_5 .

and E-plane in Fig. 10(c) and (d), respectively. As predicted, the elevation angles of the maximum radiation appear at 17.6° and 37.2° for the E-plane and H-plane, respectively, which are in accordance with the angles of M_1 and M_2 (see Fig. 9). This example demonstrates that we could alter (e.g. compress, stretch) the shape of the ring in the radiation pattern by changing the ring-shaped coding sequence in the coding pattern.

Next, we consider the combination of two different coding sequences. Fig. 11(a) shows coding pattern M_4 which is obtained by firstly adding a coding sequence S_1 that varies along the x -direction (super-unit-cell size $N = 3$) to M_1 , and then calculating the modulus of it by 8. Carefully inspecting Fig. 11(a), one may find a larger gradient of coding digits on the left side of the round area than the right side. This is due to the fact that the gradient of the added sequence S_1 is along the x -direction, which tilts the cone-shaped coding pattern to the right side. Therefore, the ring-shaped radiation pattern is expected to be also tilted to the right side with a certain angle, as is shown in Fig. 11(c), where the ring-shaped radiation pattern is shifted to the right side with negligible distortion. The ring is deflected

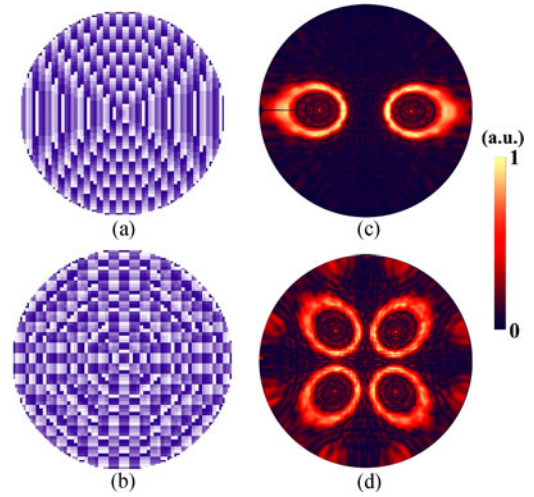


Fig. 12. (a) and (b) The coding patterns for M_6 and M_7 . (c) and (d) The 3D radiation patterns for M_6 and M_7 .

by 12.4° in the elevation plane (not shown the radiation pattern in the E-plane for brevity of content), which agrees well with the theoretical value of 12.0° . If we want to further deviate the ring-shaped radiation pattern to a larger oblique angle, we can simply reduce the super-unit-cell size to 1 for the sequence S_1 that varies along the x -direction, resulting in the mixed coding pattern M_5 in Fig. 11(b). Because of the smaller size of super-unit-cell, the coding pattern exhibits a faster changing rate of the coding digits from “0” to “7” in comparison to Fig. 11(a). The resulting ring-shaped radiation pattern is shifted accordingly to a larger angle of 38.5° , as can be observed from Fig. 11(d) and is again in strong correlation to the theoretical value of 38.6° .

Based on the aforementioned theory of combining multiple periodic coding sequences to generate new radiation patterns, we present here more complexed coding patterns that enable multiple rings in the radiation pattern. Fig. 12(a) shows the coding pattern M_6 , which is obtained from the combination of a “0404...” coding sequence (super-unit-cell size $N = 4$, denoted as S_2) that varies along the x -direction and the coding pattern M_1 . Since the S_2 sequence can split the normal incidence to two equal beams in the upper-half space, we should expect two rings to appear in the radiation pattern with equal distance to the center, as can be verified from Fig. 12(c). The coding pattern M_1 could also be added by a coding sequence that features the chessboard distribution (super-unit-cell size $N = 6$), as is shown in Fig. 12(b). From the radiation pattern of M_7 shown in Fig. 12(d), we find both the features of ring-shaped pattern and four beams split pattern. Four equal-sized ring-shaped radiation patterns are formed in four directions, with their centers located at $(\varphi = \pm 45^\circ / \pm 135^\circ, \theta = 36.1^\circ)$.

In the previous four examples, the centers of the multiple ring-shaped radiation patterns are shifted away from the z -axis ($\theta = 0^\circ$) because the gradient of the added sequences is along the x and/or y directions. Here, we present a coding scheme that could generate two concentric rings with different diameters in the radiation pattern. Fig. 13(a) shows such a coding pattern M_8 which is obtained from the addition of a coding sequence S_1

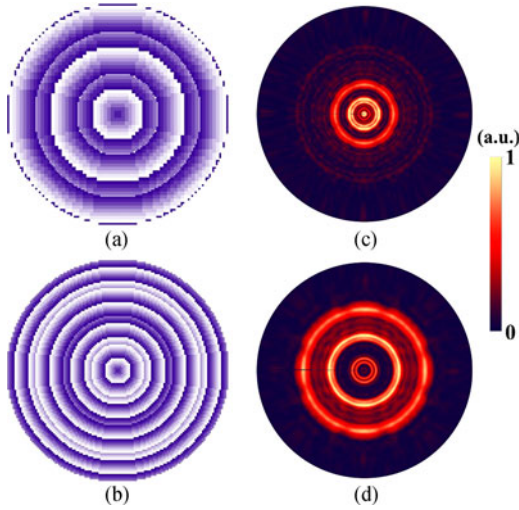


Fig. 13. (a) and (b) The coding patterns for M_8 and M_9 . (c) and (d) The 3D radiation patterns for M_8 and M_9 .

(super-unit-cell size $N = 2$) and a sequence S_2 (super-unit-cell size $N = 24$). Since the gradient of both sequences are along the radiation direction, two concentric rings can be observed from the radiation pattern in Fig. 13(c) at $\theta = 12.3^\circ$ and 24.3° . The elevation angle difference between these two rings is 12° , which corresponds exactly to the anomalous angle of 11.9° for the S_2 sequence; and the mid-value of the two elevation angles 18.3° is just equal to the theoretical value of the S_1 sequence. That is to say, the angle difference between the two rings are determined by the S_2 sequence, and their center by the S_1 sequence. This principle is further confirmed by reducing the size of super unit cell of S_1 and S_2 down to 1 and 16, respectively, resulting in the coding pattern M_9 in Fig. 13(b). As both the periodicities of the S_1 and S_2 sequences are shortened, an increase of the diameters of both rings and their difference can be observed from the radiation pattern in Fig. 13(d).

B. Implementation Using Real Structures

To demonstrate the powerful manipulations of coding metasurfaces in generating various types of ring-shaped radiation patterns with realistic structures at terahertz frequency, we design the coding particle as shown in the inset of Fig. 14(a). Similar to the structures in the previous works [43]–[46], it is also a sandwiched structure with two metallic layers and one dielectric spacer. Although this structure may look pretty much the same as the old one with square patch design [43], it has two obvious advantages over the previous structures which have only one conductor in each unit cell. First, this new structure features low EM interference between adjacent unit cells due to the existence of four additional sticks at the four edges of the coding particle. All the four sticks have the same dimension of $L_2 = 200 \mu\text{m}$ and $w = 5 \mu\text{m}$. The added sticks can be viewed as, in a sense, a common ground which isolates coding particles from each other when they are arranged in an array, and could therefore reduce the undesired EM interference between two adjacent coding particles that have different geometries. This

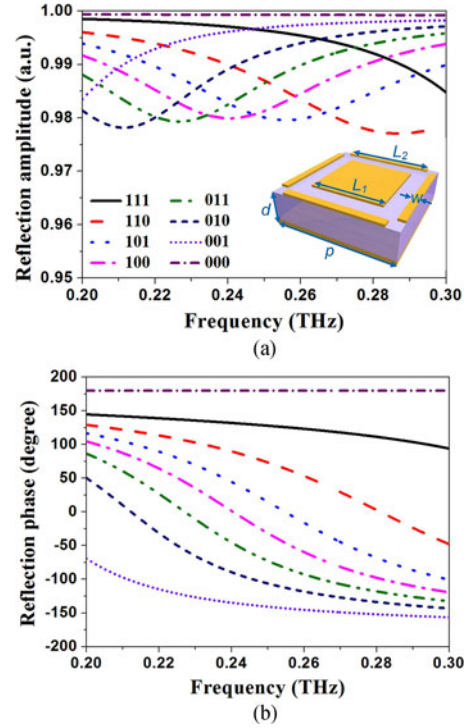


Fig. 14. (a) and (b) The numerically simulated amplitudes and phases of the eight coding particles. The inset of (a) shows the structure of the coding particle.

is in contrast to the single conductor configuration [43]–[46], in which the reflection response highly depends on the distance between its neighbors, and may deviate from the designed value. Second, the new structure has almost unity amplitude of reflection (over 0.98) because a much less lossy material, crystal quartz ($\epsilon_r = 4.4$, $\delta = 0.0004$), is adopted as the dielectric substrate with only $60 \mu\text{m}$ thickness. Owing to the extremely low loss of crystal quartz at THz frequency, it can be considered as an alternative material for the substrate of both the reflection and transmission types of coding metamaterials at terahertz frequency. Although we did not fabricate this sample in this work, we have tested the feasibility, in our previous fabrications, of reducing the thickness of a quartz substrate from $500 \mu\text{m}$ to $60 \mu\text{m}$ using the grinding and polishing processes.

To obtain the optimized geometrical parameters for the eight coding particles, we employ the frequency-domain solver of the commercial software, CST Microwave Studio, to simulate the designed structure with the Floquet boundary condition. The length L_1 of the inner square patch for the eight coding particles “000”, “001”, “010”, “011”, “100”, “101”, “110”, and “111” are optimized as 250, 227.3, 212.8, 204, 195.3, 184.5, 165, and $10 \mu\text{m}$, respectively. Fig. 14(a) and (b) show the amplitudes and phases of reflections from 0.2 to 0.3 THz for the eight coding particles, respectively. At the operating frequency 0.24 THz, the phases reach exactly to -180° , -135° , -90° , -45° , 2° , 45° , 90° , and 132° . It should be noted that the amplitudes of all eight coding particles are larger than 0.98 at the working frequency. We remark that this structure provides so far the highest efficiency among all the reflection type coding metasurfaces and the reflectarrays at the THz frequency.

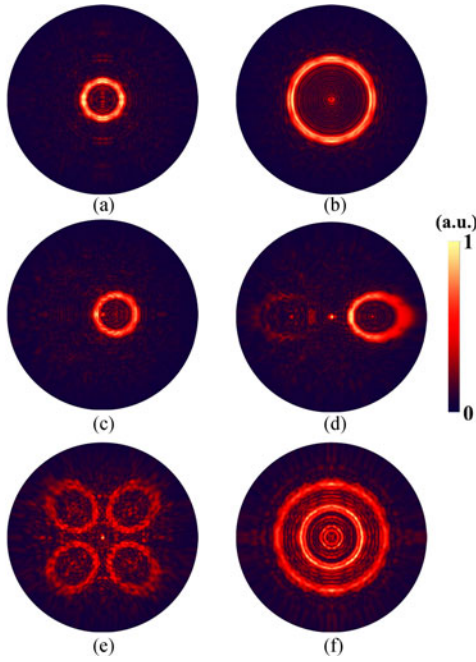


Fig. 15. (a)–(f) The 3D numerically simulated radiation patterns for M_1 , M_2 , M_4 , M_5 , M_7 and M_9 .

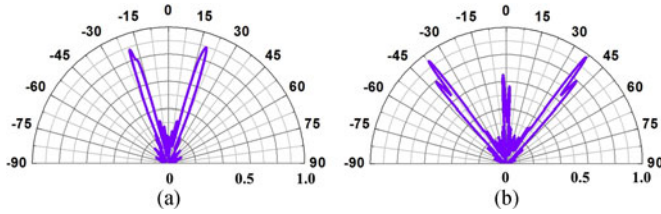


Fig. 16. (a) and (b) The 3D numerically simulated radiation patterns in the E-plane for M_1 and M_2 .

We verify the theoretical calculations by building six different coding patterns M_1 , M_2 , M_4 , M_5 , M_7 and M_9 in CST Microwave Studio using the above designed structure, and simulating them by the time-domain solver. The numerically simulated radiation patterns are shown in Fig. 15. It should be noted that the numerical results are highly consistent with the theoretical results, which verifies the correctness of the new coding scheme to generate various ring-shaped radiations, and at the same time, demonstrates the feasibility of the structure design for implementing such coding metasurfaces. Compared with the theoretical results, one may notice from Fig. 15 that more scatterings appear in the other directions besides the ring-shaped region. This should be attributed to the non-ideal reflection responses of the coding particle when they are arranged in an array, which may result in unpredictable scatterings in undesired directions.

To further characterize the angle of the ring-shaped radiations in Fig. 15(a) and (b), we plot the radiation patterns in the E-plane in Fig. 16(a) and (b), respectively. The maximum radiations for M_1 and M_2 appear at 17.6° and 38.2° , respectively, which are in excellent agreements with both the results calculated by FFT and theoretical calculations.

We should note that the ring-shaped radiation enabled by the proposed coding scheme is different from the conventional electrically small antennas which are typically implemented with the microstrip (either flat or curved) to radiate equal power at a larger range of elevation angle, resembling the shape of a doughnut. Those low directivity patterns are always employed in applications such as wireless communication, which generally requires a wide angle coverage in the elevation plane. The ring-shaped radiations presented in this work, however, could focus the EM energy in a small range of angles in the elevation plane, while at the same time, radiate equally in all azimuthal directions. By changing the periodicity of the gradient coding sequence along the radial direction, we could change the elevation angle of the cone-shaped pattern and scan the entire upper-half space using microwave. The speed for the ring-shaped pattern to scan the entire hemisphere of space is faster than the pencil beam pattern enable by the previous coding schemes [43], [46], because the ring-shaped pattern could scan all the azimuthal directions once for a given elevation angle. Although the detection range for such radiation patterns might be shorter than the pencil beam due to the relatively low directivity, it may find some applications at the microwave which requires fast scanning of the near- or medium-range of the upper-half space. Another difference of the ring-shaped pattern compared to omnidirectional antennas is that the direction, number and shape of the ring pattern can be flexibly designed. These tilted ring patterns (e.g. the pattern in Fig. 11) may be more effective for scanning a certain range of directions.

IV. CONCLUSIONS

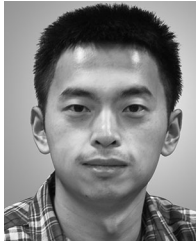
In this paper, we firstly made a review on the recent advances in coding metasurfaces, including the concepts of coding and programmable metasurfaces, broadband diffusions of terahertz waves, and anisotropic coding metasurface. We demonstrated their powerful manipulations to EM waves such as anomalous reflections, RCS reductions, linear to circular polarization, etc. In Section III, we proposed a new coding scheme that could generate ring-shaped radiation patterns. We showed the flexible control on the shape of ring-shaped radiation pattern with several different coding strategies, for example, altering the diameter of the ring by changing the periodicity of the gradient sequence along the radial direction; shifting the ring to other directions by adding it with another sequence that varies along the x or y direction, etc. A potential application of the ring-shaped radiation pattern is the capability of fast scanning of the near-medium range of the upper-half space. In the future work, we could combine the anisotropic coding metasurface [46] with this coding scheme to generate the circularly polarized ring-shaped radiation pattern.

REFERENCES

- [1] D. F. Filipovic, S. S. Gearhart, and G. M. Rebeiz, "Double-slot antennas on extended hemispherical and elliptical silicon dielectric lenses," *IEEE Trans. Microw. Theory Techn.*, vol. 41, no. 10, pp. 1738–1749, Oct. 1993.
- [2] C. A. Fernandes, "Shaped dielectric lenses for wireless millimeter wave communications," *IEEE Antennas Propag. Mag.*, vol. 41, no. 5, pp. 141–150, Oct. 1999.

- [3] P. Nayeri, F. Yang, and A. Z. Elsherbeni, "Design and experiment of a single-feed quad-beam reflectarray antenna," *IEEE Trans. Antennas Propag.*, vol. 60, no. 2, pp. 1166–1171, Feb. 2012.
- [4] S. V. Hum and J. Perruisseau-Carrier, "Reconfigurable reflectarrays and array lenses for dynamic antenna beam control: A review," *IEEE Trans. Antennas Propag.*, vol. 62, no. 1, pp. 183–198, Jan. 2014.
- [5] S. J. Wijnholds, W. A. van Cappellen, J. G. B. de Vaate, and A. van Ardenne, "Phased-array antenna system development for radio-astronomy applications," *IEEE Antennas Propag. Mag.*, vol. 55, no. 6, pp. 293–308, Dec. 2013.
- [6] R. A. Shelby, D. R. Smith, and S. Schultz, "Experimental verification of a negative index of refraction," *Science*, vol. 292, pp. 77–79, Apr. 2001.
- [7] C. G. Parazzoli, R. B. Gregor, K. Li, B. E. C. Koltenbah, and M. Tanielian, "Experimental verification and simulation of negative index of refraction using Snell's law," *Phys. Rev. Lett.*, vol. 90, Mar. 2003, Art. no. 107401.
- [8] J. B. Pendry, "Negative refraction makes a perfect lens," *Phys. Rev. Lett.*, vol. 85, pp. 3966–3969, Oct. 30, 2000.
- [9] B. Wood, J. B. Pendry, and D. P. Tsai, "Directed subwavelength imaging using a layered metal-dielectric system," *Phys. Rev. B*, vol. 74, Sep. 2006, Art. no. 115116.
- [10] R. W. Heeres and V. Zwiller, "Subwavelength focusing of light with orbital angular momentum," *Nano Lett.*, vol. 14, pp. 4598–4601, Jul. 2014.
- [11] N. Fang, H. Lee, C. Sun, and X. Zhang, "Sub-diffraction-limited optical imaging with a silver superlens," *Science*, vol. 308, pp. 534–537, Apr. 2005.
- [12] D. Schurig *et al.*, "Metamaterial electromagnetic cloak at microwave frequencies," *Science*, vol. 314, pp. 977–980, Nov. 2006.
- [13] S. Liu, H. X. Xu, H. C. Zhang, and T. J. Cui, "Tunable ultrathin mantle cloak via varactor-diode-loaded metasurface," *Opt. Express*, vol. 22, pp. 13403–13417, May 2014.
- [14] X. Ni, Z. J. Wong, M. Mrejen, Y. Wang, and X. Zhang, "An ultrathin invisibility skin cloak for visible light," *Science*, vol. 349, pp. 1310–1314, Sep. 2015.
- [15] R. Liu *et al.*, "Broadband ground-plane cloak," *Science*, vol. 323, pp. 366–369, Jan. 2009.
- [16] G. D'Aguzzo *et al.*, "Frozen light in a near-zero index metasurface," *Phys. Rev. B*, vol. 90, Aug. 2014, Art. no. 054202.
- [17] R. Maas, J. Parsons, N. Engheta, and A. Polman, "Experimental realization of an epsilon-near-zero metamaterial at visible wavelengths," *Nature Photon.*, vol. 7, pp. 907–912, Nov. 2013.
- [18] Q. Cheng, W. X. Jiang, and T. J. Cui, "Spatial power combination for omnidirectional radiation via anisotropic metamaterials," *Phys. Rev. Lett.*, vol. 108, May 23, 2012, Art. no. 213903.
- [19] D. B. Burckel *et al.*, "Micrometer-scale cubic unit cell 3D metamaterial layers," *Adv. Mater.*, vol. 22, pp. 5053–5057, Nov. 24, 2010.
- [20] T. Buckmann *et al.*, "Tailored 3D mechanical metamaterials made by dip-in direct-laser-writing optical lithography," *Adv. Mater.*, vol. 24, pp. 2710–2714, May 2012.
- [21] C. L. Holloway *et al.*, "An overview of the theory and applications of metasurfaces: The two-dimensional equivalents of metamaterials," *IEEE Antennas Propag. Mag.*, vol. 54, no. 2, pp. 10–35, Apr. 2012.
- [22] N. K. Grady *et al.*, "Terahertz metamaterials for linear polarization conversion and anomalous refraction," *Science*, vol. 340, pp. 1304–1307, Jun. 2013.
- [23] Y. Zhao, M. A. Belkin, and A. Alu, "Twisted optical metamaterials for planarized ultrathin broadband circular polarizers," *Nature Commun.*, vol. 3, May 2012, Art. no. 870.
- [24] M. Ren, E. Plum, J. J. Xu, and N. I. Zheludev, "Giant nonlinear optical activity in a plasmonic metamaterial," *Nature Commun.*, vol. 3, May 2012, Art. no. 833.
- [25] D. Shrekenhamer, J. Montoya, S. Krishna, and W. J. Padilla, "Four-color metamaterial absorber THz spatial light modulator," *Adv. Opt. Mater.*, vol. 1, pp. 905–909, Dec. 2013.
- [26] S. Liu, H. B. Chen, and T. J. Cui, "A broadband terahertz absorber using multi-layer stacked bars," *Appl. Phys. Lett.*, vol. 106, Apr. 2015, Art. no. 151601.
- [27] R. Yahiaoui, J. P. Guillet, F. de Miollis, and P. Mounaix, "Ultra-flexible multiband terahertz metamaterial absorber for conformal geometry applications," *Opt. Lett.*, vol. 38, pp. 4988–4990, Dec. 2013.
- [28] G. Zheng *et al.*, "Metasurface holograms reaching 80% efficiency," *Nature Nanotechnol.*, vol. 10, pp. 308–312, Feb. 2015.
- [29] D. D. Wen *et al.*, "Helicity multiplexed broadband metasurface holograms," *Nature Commun.*, vol. 6, Sep. 2015, Art. no. 824.
- [30] Y. W. Huang *et al.*, "Aluminum plasmonic multicolor meta-hologram," *Nano Lett.*, vol. 15, pp. 3122–3127, May 2015.
- [31] Z. W. Xie *et al.*, "Spatial terahertz modulator," *Sci. Rep.*, vol. 3, Nov. 2013, Art. no. 3347.
- [32] W. L. Chan *et al.*, "A spatial light modulator for terahertz beams," *Appl. Phys. Lett.*, vol. 94, May 2009, Art. no. 213511.
- [33] S. Savo, D. Shrekenhamer, and W. J. Padilla, "Liquid crystal metamaterial absorber spatial light modulator for THz applications," *Adv. Opt. Mater.*, vol. 2, pp. 275–279, Mar. 2014.
- [34] J. Zhang, Z. L. Mei, W. R. Zhang, F. Yang, and T. J. Cui, "An ultrathin directional carpet cloak based on generalized Snell's law," *Appl. Phys. Lett.*, vol. 103, Oct. 2013, Art. no. 151115.
- [35] X. J. Ni, Z. J. Wong, M. Mrejen, Y. Wang, and X. Zhang, "An ultrathin invisibility skin cloak for visible light," *Science*, vol. 349, pp. 1310–1314, Sep. 2015.
- [36] N. F. Yu *et al.*, "Light propagation with phase discontinuities: generalized laws of reflection and refraction," *Science*, vol. 334, pp. 333–337, Oct. 2011.
- [37] N. F. Yu *et al.*, "A broadband, background-free quarter-wave plate based on plasmonic metasurfaces," *Nano Lett.*, vol. 12, pp. 6328–6333, Dec. 2012.
- [38] F. Aieta *et al.*, "Out-of-plane reflection and refraction of light by anisotropic optical antenna metasurfaces with phase discontinuities," *Nano Lett.*, vol. 12, pp. 1702–1706, Mar. 2012.
- [39] R. Liu, T. J. Cui, D. Huang, B. Zhao, and D. R. Smith, "Description and explanation of electromagnetic behaviors in artificial metamaterials based on effective medium theory," *Phys. Rev. E*, vol. 76, Aug. 2007, Art. no. 026606.
- [40] D. R. Smith, D. Schurig, and J. J. Mock, "Characterization of a planar artificial magnetic metamaterial surface," *Phys. Rev. E*, vol. 74, Sep. 2006, Art. no. 036604.
- [41] W. J. Padilla *et al.*, "Electrically resonant terahertz metamaterials: Theoretical and experimental investigations," *Phys. Rev. B*, vol. 75, Jan. 2007, Art. no. 041102.
- [42] C. L. Holloway *et al.*, "A discussion on the interpretation and characterization of metafilms/metamaterials: The two-dimensional equivalent of metamaterials," *Metamaterials*, vol. 3, pp. 100–112, Aug. 2009.
- [43] T. J. Cui, M. Q. Qi, X. Wan, J. Zhao, and Q. Cheng, "Coding metamaterials, digital metamaterials and programmable metamaterials," *Light-Sci. Appl.*, vol. 10, Oct. 2014, Art. no. e218.
- [44] L. H. Gao *et al.*, "Broadband diffusion of terahertz waves by multi-bit coding metasurfaces," *Light-Sci. Appl.*, vol. 4, Sep. 2015, Art. no. e324.
- [45] L. J. Liang *et al.*, "Anomalous terahertz reflection and scattering by flexible and conformal coding metamaterials," *Adv. Opt. Mater.*, vol. 3, pp. 1374–1380, Oct. 2015.
- [46] S. Liu *et al.*, "Anisotropic coding metamaterials and their powerful manipulation to differently polarized terahertz waves," *Light-Sci. Appl.*, vol. 5, May 2016, Art. no. e16076.
- [47] S. Liu *et al.*, "Convolution operations on coding metasurface to reach flexible and continuous controls of terahertz beams," *Adv. Sci.*, vol. 3, Jul. 7, 2016, Art. no. 1600156. [Online]. <http://dx.doi.org/10.1002/advs.201600156>
- [48] T. J. Cui, S. Liu, and L. L. Li, "Information entropy of coding metasurface," *Light-Sci. Appl.*, vol. 5, 2016, Art. no. e16172.
- [49] P. Nayeri, F. Yang, and A. Z. Elsherbeni, "Beam-scanning reflectarray antennas a technical overview and state of the art," *IEEE Antennas Propag. Mag.*, vol. 57, no. 4, pp. 32–47, Aug. 2015.
- [50] C. Pfeiffer and A. Grbic, "Millimeter-wave transmitarrays for wavefront and polarization control," *IEEE Trans. Microw. Theory Techn.*, vol. 61, no. 12, pp. 4407–4417, Dec. 2013.
- [51] H. T. Chen *et al.*, "A metamaterial solid-state terahertz phase modulator," *Nature Photon.*, vol. 3, pp. 148–151, Feb. 2009.
- [52] Y. Zhao *et al.*, "Structural, electrical, and terahertz transmission properties of VO2 thin films grown on c-, r-, and m-plane sapphire substrates," *J. Appl. Phys.*, vol. 111, Mar. 2012, Art. no. 053533.
- [53] Y. H. Zhu *et al.*, "Tunable dual-band terahertz metamaterial bandpass filters," *Opt. Lett.*, vol. 38, pp. 2382–2384, Jul. 2013.
- [54] C. D. Giovampaola and N. Engheta, "Digital metamaterials," *Nature Mater.*, vol. 13, pp. 1115–1121, Sep. 2014.
- [55] X. Wan, M. Q. Qi, T. Y. Chen, and T. J. Cui, "Field-programmable beam reconfiguring based on digitally-controlled coding metasurface," *Sci. Rep.*, vol. 6, 2016, Art. no. 20663.
- [56] Y. Fan, X. L. Quan, Y. Pan, Y. H. Cui, and R. L. Li, "Wideband omnidirectional circularly polarized antenna based on tilted dipoles," *IEEE Trans. Antennas Propag.*, vol. 63, no. 12, pp. 5961–5966, Dec. 2015.

- [57] Y. M. Cai, S. Gao, and Y. Z. Yin, "Compact-size low-profile wideband circularly polarized omnidirectional patch antenna with reconfigurable polarizations," *IEEE Trans. Antennas Propag.*, vol. 64, no. 5, pp. 2016–2021, May 2016.
- [58] K. P. Wei, Z. J. Zhang, and Z. H. Feng, "Leaky-wave antenna array with horizontally polarized omnidirectional pattern," *IEEE Trans. Antennas Propag.*, vol. 60, no. 7, pp. 3165–3173, Jul. 2012.
- [59] S. W. Liao, Y. Peng, and Q. Xue, "Ka-band omnidirectional high gain stacked dual bicone antenna," *IEEE Trans. Antennas Propag.*, vol. 64, no. 1, pp. 294–299, Jan. 2016.



Shuo Liu received the B.E. degree in the information engineering from the School of Information Science and Engineering, Southeast University, Nanjing, China, in 2010. He is currently working toward the Ph.D. degree at the State Key Laboratory of Millimeter Waves, Department of Radio Engineering, Southeast University, Nanjing.

His research interests include metamaterials, metasurfaces, spoof surface plasmon polaritons, and wireless power transfer.



Tie Jun Cui (M'98–SM'00–F'15) received the B.Sc., M.Sc., and Ph.D. degrees in electrical engineering from Xidian University, Xi'an, China, in 1987, 1990, and 1993, respectively. In March 1993, he joined the Department of Electromagnetic Engineering, Xidian University, and became an Associate Professor in November 1993. From 1995 to 1997, he was a Research Fellow with the Institut für Hochfrequenztechnik und Elektronik, University of Karlsruhe, Karlsruhe, Germany. In July 1997, he joined the Center for Computational Electromagnetics, Department

of Electrical and Computer Engineering, University of Illinois at Urbana-Champaign, first as a Postdoctoral Research Associate and then a Research Scientist. In September 2001, he became a Cheung-Kong Professor with the Department of Radio Engineering, Southeast University, Nanjing, China, where he is the Associate Dean of the School of Information Science and Engineering, and the Associate Director of the State Key Laboratory of Millimeter Waves. Since 2013, he has been a Representative of People's Congress of China. He is a Co-Editor of the book entitled *Metamaterials—Theory, Design, and Applications* (Springer, 2009) and the author of six book chapters. He has published more than 400 peer-reviewed journal papers in *Science*, *PNAS*, *Nature Communications*, *Physical Review Letters*, and many IEEE Transactions. His research interests include metamaterials, computational electromagnetic, wireless power transfer, and millimeter wave technologies, which have been cited by more than 13 500 times.

Dr. Cui received a Research Fellowship from Alexander von Humboldt Foundation, Bonn, Germany, in 1995, and a Young Scientist Award from the International Union of Radio Science in 1999. He was awarded a Cheung Kong Professor under Cheung Kong Scholar Program by the Ministry of Education, China, in 2001, received the National Science Foundation of China for Distinguished Young Scholars in 2002, received Special Government Allowance awarded by the Department of State, China, in 2008, received the Award of Science and Technology Progress from Shaanxi Province Government in 2009, was awarded by a May 1st Labour Medal by Jiangsu Province Government in 2010, received the First Prize of Natural Science from Ministry of Education, China, in 2011, and received the Second Prize of National Natural Science, China, in 2014. His research works have been selected as one of the "10 Breakthroughs of China Science in 2010," "Best of 2010" in *New Journal of Physics*, *Research Highlights in Europhysics News*, *Journal of Physics D: Applied Physics*, *Applied Physics Letters*, and *Nature China*. His work has been reported by *Nature News*, *Science*, *MIT Technology Review*, *Scientific American*, *New Scientists*, etc. According to ELSEVIER, he is one of the Most Cited Chinese Researchers. He is an active reviewer for *Science*, *Nature Materials*, *Nature Photonics*, *Nature Physics*, *Nature Communications*, *Physical Review Letters*, *Advanced Materials*, and a series of IEEE Transactions. He was an Associate Editor of the IEEE TRANSACTIONS ON GEOSCIENCE AND REMOTE SENSING and a Guest Editor in *Science China Information Sciences*. He served as an Editorial Staff in IEEE ANTENNAS AND PROPAGATION MAGAZINE, and is in the editorial boards of *Progress in Electromagnetic Research* and *Journal of Electromagnetic Waves and Applications*. He served as the General Co-Chair of the International Workshops on Metamaterials in 2008 and 2012, the TPC Co-Chair of Asian Pacific Microwave Conference in 2005, and Progress in Electromagnetic Research Symposium in 2004.